Thermal Conductivity of Snow, Firn, and Porous Ice From 3-D Image-Based Computations

Neige Calonne, Lucas Milliancourt, Alexis Burr, Armelle Philip, Christophe L. Martin, Frédéric Flin, Christian Geindreau

AGU100 ADVANCING EARTH AND SPACE SCIENCE

Geophysical Research Letters

RESEARCH LETTER
10.1029/2019GL085228

Thermal Conductivity of Snow, Firn, and Porous Ice From 3-D Image-Based Computations

Neige Calonne[1], Lucas Milliancourt[2,3], Alexis Burr[2,4], Armelle Philip[2], Christophe L. Martin[4], Frederic Flin[1], and Christian Geindreau[3]

[1]Université Grenoble Alpes, Université de Toulouse, Météo-France, CNRS, CNRM, Centre d'Études de la Neige, Grenoble, France, [2]Grenoble INP Institute of Engineering, IGE, Université Grenoble Alpes, CNRS, IRD, Grenoble, France, [3]Grenoble INP Institute of Engineering, 3SR, Université Grenoble Alpes, CNRS, Grenoble, France, [4]Grenoble INP Institute of Engineering, SIMaP, Université Grenoble Alpes, CNRS, Grenoble, France

Key Points:
- Snow-designed predictive formulas significantly underestimate the thermal conductivity when applied to firn and porous ice
- Thermal conductivity of firn and porous ice is isotropic and linearly correlated to density
- We present a new formula for the thermal conductivity of snow, firn, and porous ice based on density and temperature

Supporting Information:
- Supporting Information S1

Correspondence to:
N. Calonne,
neige.calonne@meteo.fr

Citation:
Calonne, N., Milliancourt, L., Burr, A., Philip, A., Martin, C. L., Flin, F., & Geindreau, C. (2019). Thermal conductivity of snow, firn, and porous ice from 3-D image-based computations. *Geophysical Research Letters*, *46*, 13,079–13,089. https://doi.org/10.1029/2019GL085228

Received 30 AUG 2019
Accepted 30 OCT 2019
Accepted article online 13 NOV 2019
Published online 16 NOV 2019

Abstract Estimating thermal conductivity of snow, firn, and porous ice is key for modeling the thermal regime of alpine and polar glaciers. Whereas thermal conductivity of snow was widely investigated, studies on firn and porous ice are very scarce. This study presents the effective thermal conductivity tensor computed from 64 3-D images of microstructures of snow, antarctic firn, and porous ice at −3, −20, and −60°C. We show that, in contrast with snow, conductivity of firn and porous ice correlates linearly with density, is approximately isotropic, and is largely impacted by temperature. We report that performances of commonly used estimates of thermal conductivity vary largely with density. In particular, formulas designed for snow lead to significant underestimations when applied to denser ice structures. We present a new formulation to accurately estimate the thermal conductivity throughout the whole density range, from fresh snow to bubbly ice, and for any temperature conditions encountered in glaciers.

Plain Language Summary Understanding how temperature fluctuations are propagated through snow, firn, and porous ice is crucial for many applications related to alpine and polar glaciers. Whereas thermal conductivity of snow was widely investigated, studies on firn and porous ice are very scarce. This study provides the effective thermal conductivities computed from 64 3-D images of microstructures of snow, antarctic firn, and porous ice at temperatures of −3, −20, and −60°C. For the first time, the evolution of thermal conductivity over the full range of density is revealed, from fresh snow, with up to 80% of air, to bubbly ice, with less than 10% of air. We show that, in contrast with snow, thermal conductivity of firn and porous ice correlates linearly with density, is approximately isotropic, and is largely impacted by temperature. Assessing some commonly used predictive formulas of thermal conductivity of snow, firn, and porous ice, we found that none allowed for robust estimations throughout the full density range. In particular, formulas designed for snow lead to significant underestimations when applied to denser ice structures. We present a new density- and temperature-based formula to accurately estimate thermal conductivity of snow, firn, and porous ice in alpine or polar conditions.

1. Introduction

Many glaciers and ice sheets processes depend on thermal conditions: surface snow metamorphism, firn densification, ice deformation, or basal sliding, for instance. How temperature fluctuations are propagated through snow, firn, and porous ice is therefore crucial to understand, as its modeling is required in a variety of applications such as the interpretation of paleoclimatic data from ice cores (e.g., Barnola et al., 1991; Goujon et al., 2003; Salamatin et al., 1998; Schwander et al., 1997), past climate reconstruction from temperature profiles (e.g., Dahl-Jensen et al., 1998; Gilbert et al., 2010; Gilbert & Vincent, 2013; Van Ommen et al., 1999), interpretation of englacial temperature observation (e.g., Funk et al., 1994; Gilbert et al., 2014; Lüthi & Funk, 2001), climate-cryosphere interactions studies and future scenarios (e.g., Gilbert et al., 2014, 2016; Seddik et al., 2012), glacier hazard assessment (e.g., Gilbert et al., 2015, 2018), or ice mass balance monitoring (e.g., Cummings et al., 2013; Reijmer & Hock, 2008).

Snow thermal conductivity was largely investigated based on field and laboratory experiments, and several quadratic or exponential density-based regressions were proposed (Fukusako, 1990; Satyawali & Singh, 2008; Schneebeli & Sokratov, 2004; Sturm et al., 1997; Yen, 1981). A large scatter was however often reported when

plotting conductivity versus density, which was attributed to additional influences of the snow microstructure other than density and also to different measurements biases (see, e.g., Calonne et al., 2011; Morin et al., 2012). In addition, experimental values of thermal conductivity often correspond to *apparent* thermal conductivities, which characterize all the heat transport processes involved and not purely conduction. Overcoming the experimental issues, numerical simulations on 3-D tomographic images of snow microstructures allowed to retrieve the *effective* thermal conductivity tensor (Calonne et al., 2011; Kaempfer et al., 2005). The term *effective* refers to the property of a composite material as defined in material sciences (e.g., Kanit et al., 2006). Anisotropy of the thermal conductivity tensor could then be quantified and appeared to be significant for some snow types, implying enhanced heat conduction in particular directions (Calonne et al., 2011; 2014; Löwe et al., 2013). Differences up to a factor 2 between the vertical and the horizontal components were reported for depth hoar (Riche & Schneebeli, 2013). This anisotropy was correlated with the structural anisotropy of the snow microstructure. Such microstructures, preferentially arranged in one direction, will exhibit higher conductivity values along that direction. Thermal conductivity of snow increases overall with decreasing temperature, although variations are nonlinear and depend on density (the denser, the larger the influence) (Calonne et al., 2011; Sturm et al., 1997). They result from the variations of the air and ice thermal conductivity themselves with temperature, which are opposite and of different magnitude.

Data on thermal conductivity of firn and porous ice are very scarce: Giese and Hawley (2015) provide a single bulk value of the top first 30 m of firn at Summit, Greenland, and Marchenko et al. (2019) present eight vertical profiles of firn conductivity of 10 m depth and 1 m resolution at Lomonosovfonna, Svalbard. In both studies, thermal conductivity is obtained by best matching modeled temperature profiles to in situ measured ones. A linear correlation between density and conductivity is found but comes with a large scatter, which is attributed to measurement errors (Marchenko et al., 2019). The microstructure of firn and porous ice can be noticeably different at a given density because of the different thermomechanical constraints they underwent (Burr et al., 2018, 2019; Lomonaco et al., 2011). Its influence was however never investigated.

Because of the lack of data and dedicated predictive formulas, thermal conductivity of firn and porous ice is often estimated based on parameterizations actually designed for snow, that is, for densities between 100 and 550 kg/m^3, without being able to evaluate their performances at higher densities. Marchenko et al. (2019) indicate that snow-designed parameterizations may underestimate firn conductivity. As summarized in Table 1, some of the most commonly used formulas to model heat conduction in glaciers are the following:

- the average of the Van Dusen and the Swcherdtfeger formulas, often described as lower and upper limits, respectively (Paterson, 1994) (e.g., used in, Humphrey et al., 2012; Lüthi & Funk, 2001; Van Ommen et al., 1999)
- the Yen formula (e.g., used in, Arthern & Wingham, 1998; Cummings et al., 2013)
- the Sturm formula (e.g., used in, Reijmer & Hock, 2008; Zwinger et al., 2007)
- the Schwander formula (e.g., used in, Goujon et al., 2003)
- the Calonne formula (e.g., used in, Gilbert & Vincent, 2013; Gilbert et al., 2014)

Most of these predictive formulas were developed for a given temperature range (Table 1). To estimate thermal conductivity at temperatures outside of the given range, a multiplicative factor accounting for the variations of the ice thermal conductivity with temperature, neglecting the variations in air, is often applied (e.g., Gilbert et al., 2014; Schwander et al., 1997; Zwinger et al., 2007). In contrast, some models of heat transfer assume constant density and temperature, relying on constant values of thermal conductivity (e.g., Hills et al., 2018; Larour et al., 2012).

The aim of this paper is to extend our knowledge on effective thermal conductivity, up to now limited to snow, to denser ice structures, using the 3-D images-based computation technique. To do so, we used 27 3-D images of antarctic firn and porous ice microstructures complemented by 37 3-D images of seasonal snow microstructures, covering a density range from 100 to 888 kg/m^3. The evolution of the thermal conductivity tensor with density, variations with temperature between −3, −20, and −60°C, and tensor anisotropy are first discussed. Comparisons with previous data sets as well as estimates from common parameterizations and standard models are then presented. A new predictive formula, valid for fresh snow to bubbly ice, is finally proposed.

Table 1
Main Characteristics and Description of Commonly Used Formulas to Predict Thermal Conductivity of Snow, Firn, and Ice

Name	Formula	Density ρ (kg/m^3)	Temperature (°C)	Comments
Yen	$k_{yen} = 2.22362\left(\frac{\rho}{1000}\right)^{1.885}$	80–600	not defined	regression on experimental measurements data (Yen, 1981).
Calonne	$k_{cal.} = 0.024–1.23\times10^{-4}\rho + 2.5\times10^{-6}\rho^2$	100–550	−3°C	regression on 3-D images-based computations data (Calonne et al., 2011).
Sturm	$k_{sturm} = 0.023 + 0.234\,\frac{\rho}{1000}$ for $\rho < 156$ $k_{sturm} = 0.138–1.01\,\frac{\rho}{1000} + 3.233\left(\frac{\rho}{1000}\right)^2$ for $156 < \rho < 600$	70–560	−1 to −77°C (average −15°C)	regression on needle probe measurements data (Sturm et al., 1997).
Van Dusen	$k_{vd} = 2.1\times10^{-2} + 4.2\times10^{-4}\rho + 2.2\times10^{-9}\rho^3$	"snow"	0 to −30°C	regression on experimental measurements data (Van Dusen & Washburn, 1929).
Schwerdtfeger	$k_{schwerd.} = \frac{2\rho}{3\rho_i - \rho}k_i$	"dense snow to bubbly ice"	full range	analytical formula (Schwerdtfeger, 1963).
Schwander	$k_{schwander} = k_i\left(\frac{\rho}{\rho_i}\right)^{2-0.5\frac{\rho}{\rho_i}}$	full range	full range	combines a regression on experimental data (Mellor, 1977) and the Schwerdtfeger formula (Schwander et al., 1997).

2. Instruments and Methods

2.1. 3-D Images

This study is based on a set of 64 3-D images that includes 37 images of snow samples and 27 images of firn and porous ice samples, all from previous studies. Firn samples are subsamples of Antarctic ice cores from three locations: Dome C, near Concordia Station (75°6′S, 123°21′E); Lock In, located at 136 km away from Concordia Station (74°8.310′S, 126°9.510′E); and Vostok, obtained during different previous expeditions (Burr et al., 2018; Coléou & Barnola, 2001; Gautier et al., 2016). They were extracted at depths ranging from 23 to 133 m, covering different levels of densification until the close-off. Snow samples originate from previous field samplings or controlled cold-laboratory experiments (Calonne et al., 2014; Coléou et al., 2001; Flin et al., 2004, 2011). The main seasonal snow types as defined by the international classification of seasonal snow grains (ICSSG) (Fierz et al., 2009) are represented. The 3-D images are binary images (air or ice) of resolutions between 5 and 15 μm and of dimensions between 2.5^3 and $7^2 \times 25$ mm^3. Details on samples preparation and image acquisition as well as the reference papers can be found in Table S1 of the supporting information.

2.2. Effective Thermal Conductivity Tensor

The full 3-D tensors of effective thermal conductivity $\mathbf{k}$ (W·m^{-1}·K^{-1}) were computed from the 3-D images of the 64 samples of this study, following the method described by Calonne et al. (2011). A specific boundary value problem arising from a homogenization technique (Auriault et al., 2009; Calonne et al., 2014) is solved on representative elementary volumes extracted from the 3-D images for given values of air conductivity k_a and ice conductivity k_i. We used the software Geodict, which is based on finite difference method (Thoemen et al., 2008). Here, we performed computations at −3, −20, and −60°C using k_i = 2.107, 2.330, and 2.900 W·m^{-1}·K^{-1} and k_a = 0.024, 0.023, and 0.019 W·m^{-1}·K^{-1}, respectively, following Paterson (1994) for the ice conductivity values and Yen (1981) for the air conductivity values. As the nondiagonal terms of the tensor $\mathbf{k}$ are negligible, we consider only the diagonal terms k_x, k_y, k_z, which correspond to the eigenvalues of $\mathbf{k}$ (the image axes x, y, and z correspond to the principal directions of the microstructure, z being along the direction of gravity). Besides, $k_x \simeq k_y$, so $\mathbf{k}$ is transversely isotropic. We refer to k as the average of the diagonal terms of $\mathbf{k}$, to k_z as the vertical component, and to k_{xy} as the horizontal component defined as the average of k_x and k_y. Anisotropy of the thermal conductivity tensor is analyzed based on the anisotropy ratio defined as $\mathcal{A}_k = k_z/k_{xy}$ (e.g., Calonne et al., 2011, 2014; Riche & Schneebeli, 2013).

2.3. Density, Correlation Lengths, and Structural Anisotropy

Density ρ (kg/m^3) was computed from 3-D images by a standard voxel counting algorithm using an ice density of ρ_i of 917 kg/m^3 (ice density variations with temperature were neglected in this study). Correlation

lengths l_{c_x}, l_{c_y}, and l_{c_z} (mm) were used as a characteristic length of the ice and pore structure in the x, y, and z directions, respectively. They were obtained by first computing from 3-D images the two-point correlation functions $S_2(\mathbf{r}_\beta)$ for the air phase, $\mathbf{r}_\beta$ being a vector oriented along the coordinate axes $\beta = (x, y, z)$ of length $|\mathbf{r}_\beta| = r_\beta$ ranging from 0 to the image size in the β direction with increments of 1 pixel size (Torquato, 2002). Correlation lengths l_{c_β} were then obtained by fitting the two-point correlation functions to an exponential equation of form $S_2(r_\beta) = (\phi - \phi^2)\exp(-r_\beta/l_{c_\beta}) + \phi^2$ where $\phi = 1 - \frac{\rho}{\rho_i}$ is the porosity (Calonne et al., 2014; Löwe et al., 2013). As snow is a transversely isotropic material, the structural anisotropy of the microstructure was then characterized based on the ratio $\mathcal{A}_{l_c} = l_{c_z}/l_{c_{xy}}$, where $l_{c_{xy}}$ is the mean of l_{c_x} and l_{c_y}.

3. Results and Discussion

3.1. Evolution With Density at −3°C

The evolution of the vertical and horizontal components of the effective thermal conductivity tensor at −3°C as a function of density is presented in Figure 1a. Averaged values range from 0.06 $W{\cdot}m^{-1}{\cdot}K^{-1}$, for a precipitation particles sample of density 102 kg/m^3, to 2.00 $W{\cdot}m^{-1}{\cdot}K^{-1}$, for the porous ice sample extracted at 133 m depth at Dome C of density 888 kg/m^3. The strong dependency of conductivity with density is clearly highlighted. The quadratic relationship observed for snow smoothly transitions into a linear relationship for firn and porous ice. The transition seems to occur around 450 kg/m^3. Above that, a change in density proportionally translates into a change in thermal conductivity, independently of the considered density. Below that, the same change in density leads to smaller changes of thermal conductivity, which depend on the considered density. This behavior of the conductivity-density relationship is related to the high contrast between the thermal conductivity of air and ice combined with morphological effects of the microstructure. At low densities, ice grains are insulated by the predominant surrounding pore space. The few bonds between ice grains play then a critical role in the overall heat conduction as they act as heat paths. Hence, during a change in density, the portion of ice added or removed elsewhere than at ice bonds has little impact on the overall heat conduction. This portion of "inefficient" ice results in a reduced change in the effective thermal conductivity. As structures get denser and more connected, the portion of "inefficient" ice decreases, so the impact of a density change on thermal conductivity gets larger, as shown from light to dense snow (Figure 1a). The portion of "inefficient" ice finally vanishes at higher densities, from about 450 kg/m^3. Changes in density translate then into proportional changes in thermal conductivity.

Fitting conductivity and density of the firn and porous ice samples at −3°C, and constraining a value of 2.107 $W{\cdot}m^{-1}{\cdot}K^{-1}$ at 917 kg/m^3, we obtained the following linear regression:

$$k_{\text{firn}} = 2.107 + 0.003618(\rho - \rho_i) \tag{1}$$

with a R^2 of 0.99 and a standard deviation lower than 10^{-5} $W{\cdot}m^{-1}{\cdot}K^{-1}$. This regression is valid in the range 550–917 kg/m^3 and can be used for firn, porous ice, and pure ice. Plotting the data in a vertical profile, the deeper the firn and ice samples, the denser the samples and the higher the conductivity (Figure 2a). Between 23 to 133 m depth, density evolves from 566 to 888 kg/m^3, and averaged thermal conductivity at −3°C evolves from 0.87 to 2 $W{\cdot}m^{-1}{\cdot}K^{-1}$.

3.2. Variation With Temperature

Results described above are valid for a rather warm environment (−3°C). Temperatures in glaciers fluctuate and can reach very low temperatures. At Dome C for example, surface temperatures vary between −25°C in summer and −70°C in winter, whereas temperature at 5 m depth is about −55°C year-around (Brucker et al., 2011). Overall thermal conductivity increases with decreasing temperature (Figures 1b and 2a), following the dependency of pure ice conductivity (Calonne et al., 2011; Paterson, 1994; Sturm et al., 1997; Yen, 1981). The thermal conductivity of the Vostok firn sample of density 774 kg/m^3 increases by a factor 1.4 between −3 and −60°C for instance (from 1.6 to 2.2 $W{\cdot}m^{-1}{\cdot}K^{-1}$). Variations depend however on density in a nonlinear manner. Firn and porous ice above 600 kg/m^3 are affected the most: variations of their thermal conductivity with temperature actually correspond approximately to the one in pure ice. Increase is about 37% from −3 to −60°C and of 10% from −3 to −20°C. Those variations decrease to about 20% and 5% at 300 kg/m^3, for both temperature fluctuations, respectively, and become negligible at lower densities. At very low densities, variations even change direction and our lightest snow sample of 102 kg/m^3 shows a thermal conductivity 4% larger at −3°C than at −60°C.

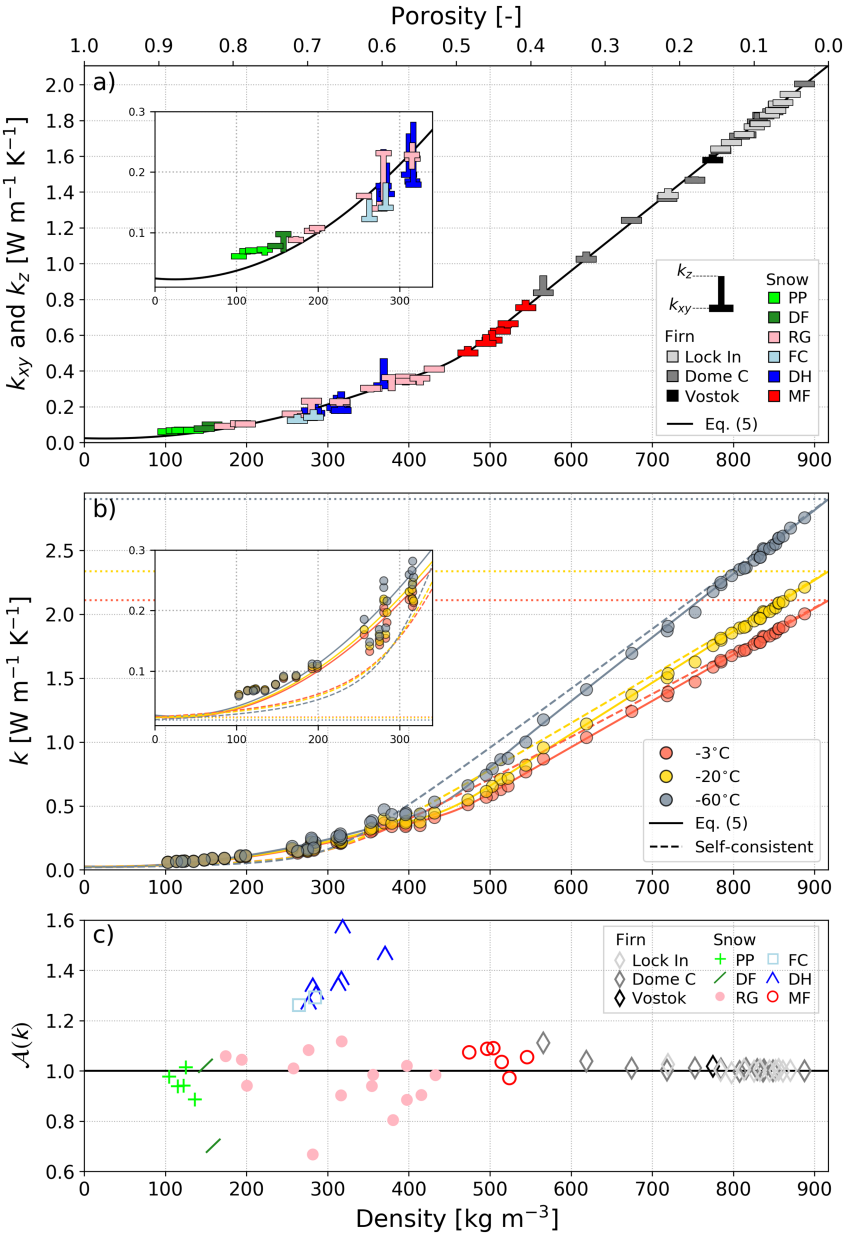

Figure 1. Effective thermal conductivity versus density: (a) horizontal and vertical components k_{xy} and k_z at −3°C, (b) averaged values k at −3, −20, and −60°C, and (c) anisotropy ratio $\mathcal{A}_k$ at −3°C. Estimates from the new formulation equation (5) and the SC model are also shown. Snow types correspond to the ICSSG (Fierz et al., 2009): precipitation particles (PP), decomposed and fragmented particles (DF), rounded grains (RG), faceted crystals (FC), depth hoar (DH), and melt forms (MF). Air and ice thermal conductivities at −3, −20, and −60°C are indicated in dotted lines in (b).

3.3. Anisotropy

Looking closely at the T-shaped symbols in Figure 1a, differences between the horizontal and vertical components of the thermal conductivity can be found but tend to vanish above 600 kg/m^3. No or very little anisotropy is indeed observed for firn and porous ice samples, with most anisotropy ratio $\mathcal{A}_k$ close to 1 (Figure 1c). Anisotropy tends overall to vanish with density and depth, the highest anisotropy of firn of 1.11 being shown for a Dome C sample collected at 23 m depth of density 565 kg/m^3. This indicates that a single orientationally averaged value of thermal conductivity is sufficient to describe heat conduction in any direction of firn and porous ice. In contrast, ratios observed for snow vary largely, independently on density (Figure 1c). Besides, anisotropy of the thermal conductivity of snow is overall well correlated with the anisotropy of the correlation length: $\mathcal{A}_k$ ranges from 0.66 for a rounded grains sample with a $\mathcal{A}_{l_c}$ of 0.67,

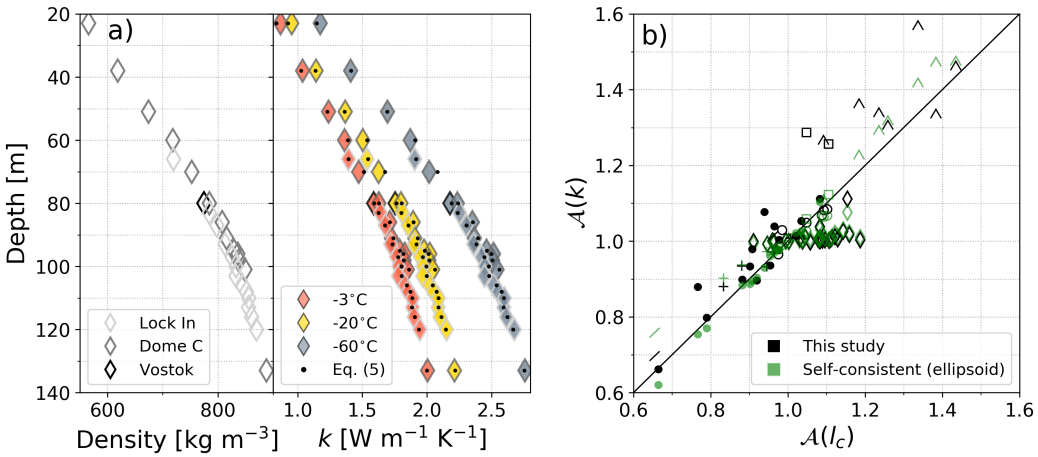

Figure 2. (a) Density and averaged thermal conductivity evolution with depth computed from 3-D images (diamonds) and estimated from equation (5) (dots) at −3, −20, and −60°C. (b) Anisotropy ratio of the thermal conductivity at −3°C versus anisotropy ratio of the correlation length computed from 3-D images (black color) and estimated from the SC model with ellipsoidal inclusions equations (3) and (4) (green color). Firn samples are shown by diamonds, and snow samples are shown using the symbols of the ICSSG as in Figure 1c.

to 1.57 for a depth hoar sample with a $\mathcal{A}_{l_c}$ of 1.34 (Figure 2b). This highlights the influence of the structural anisotropy of the microstructure on conductivity, as previously reported (Calonne et al., 2014; Löwe et al., 2013). Such a correlation is not observed for firn and porous ice, for which variations of $\mathcal{A}_{l_c}$, ranging from 0.91 to 1.19, do not coincide with the almost invariant $\mathcal{A}_k$ around 1 (Figure 2b). This implies that at high density the influence of the structural anisotropy, which refers mostly to the shape of the pore spaces embedded in the dominant portion of ice, becomes insignificant for heat conduction.

3.4. Comparison With Other Data

We compare now our values of thermal conductivity with the data of Marchenko et al. (2019) and Giese and Hawley (2015) presented in section 1 (Figure 3a). Authors reported temperatures fluctuating between −15 and −40°C at the Summit site (Giese & Hawley, 2015) and between 0 and −20°C at the Lomonosovfonna site (Marchenko et al., 2019). We thus plotted here our results at −20°C, as the more relevant to be compared with. General trends are in agreement but data of Marchenko et al. (2019) shows more scatter and overall larger values than ours. As discussed by the authors, the scatter likely reflects uncertainties related to measurement deviations or vertical mismatches between density profiles and temperature profiles.

3.5. Comparison With Predictive Formulas

3.5.1. Estimates at −3°C

Next, we evaluate the performance of the commonly used parameterizations listed in Table 1. In addition, we evaluate an analytical homogenization method called the self-consistent (SC) approximation for spherical inclusions (Bruggeman, 1935; Hill, 1965; Torquato, 2002). It provides thermal conductivity estimates k_{sc} based on density along with the air and ice conductivity and is defined as

$$k_{sc} = \frac{\alpha + \sqrt{\alpha^2 + 4(d-1)k_i k_a}}{2(d-1)}$$
$$\text{with} \quad \alpha = k_i\left(d\frac{\rho}{\rho_i} - 1\right) + k_a\left(d\left(1 - \frac{\rho}{\rho_i}\right) - 1\right) \quad \text{and} \quad d = 3. \tag{2}$$

We compare first the different estimations with our results at −3°C in Figure 3b. Values of error, relative error, and standard deviation can be found in the supporting information (Table S2 and Figure S1). All the snow-designed formulas (Yen, Sturm, and Calonne) perform rather poorly for firn and porous ice above 550 kg/m^3, for which a significant underestimation is found with errors ($k_{\text{estimated}} - k$) between −0.1 and −0.3 W·m^{-1}·K^{-1}, whereas k ranges from 0.8 to 2.0 W·m^{-1}·K^{-1} in this density range. This leads to relative errors ($k_{\text{estimated}} - k$)/k between about −12% to −30%. Note that the underestimation is also true at lower densities for the Sturm formula (see, Calonne et al., 2011; Morin et al., 2013 for details). On the other hand, the mean Van Dusen–Schwerdtfeger largely overestimates the thermal conductivity within the snow density range (100–550 kg/m^3) with errors up to 0.2 W·m^{-1}·K^{-1} and relative errors exceeding 100%. Overall,

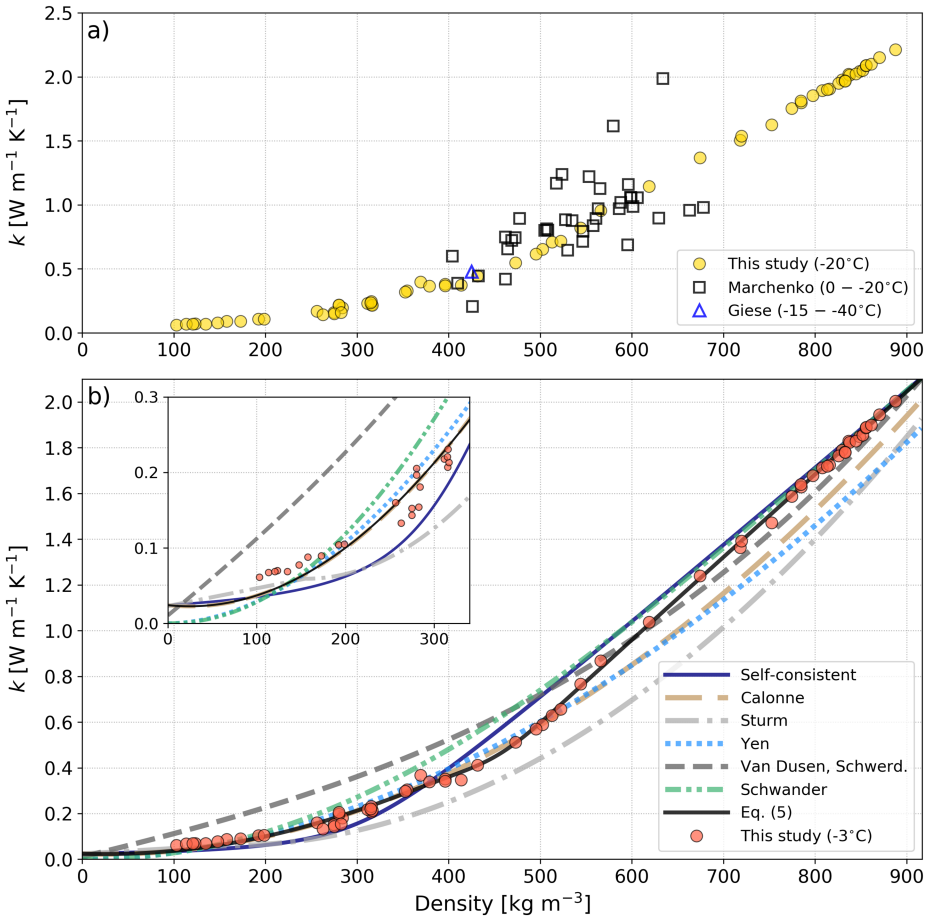

Figure 3. Comparison of the evolution of the thermal conductivity with density between (a) our computations at −20°C and the data of Giese and Hawley (2015) and Marchenko et al. (2019), and (b) our computations at −3°C and estimates from the commonly used parameterizations described in Table 1, the SC model, as well as equation (5). The bulk thermal diffusivity provided by Giese and Hawley (2015) (25 m^2/year) was converted in terms of thermal conductivity (0.48 $W{\cdot}m^{-1}{\cdot}K^{-1}$) using a bulk density of 425 kg/m^3 and a density-dependent specific heat capacity at −30°C of 1,412 $J{\cdot}kg^{-1}{\cdot}K^{-1}$.

the SC model and the Schwander formula provide estimates closest to our data. Still, their performances are not consistent with density. For instance, between 100 and 200 kg/m^3 the SC model underestimates the thermal conductivity by about −40% and the Schwander formula overestimates it by 25% to 50% in the range 250–450 kg/m^3. Moreover, none of the models is able to accurately reproduce the thermal conductivity of light snow with densities below 150 kg/m^3. Relative errors from all the models are over ±25%, and up to around −40% for the SC model, Calonne, Yen, and Schwander formulas (not to mention the mean Van Dusen–Schwerdtfeger). The corresponding errors are of the order of 0.02 $W{\cdot}m^{-1}{\cdot}K^{-1}$. Although this could appear insignificant, a factor 0.75 to 0.6 on the thermal conductivity of low-conductive snow layers, acting as insulating barriers, can impact greatly the overall heat transfer in some cases (Calonne et al., 2011).

3.5.2. Temperature Effects

Next, we assessed the modeling of the thermal conductivity variations with temperature. As introduced earlier, this effect is classically taken into account through the variations of the pure ice conductivity with temperature, neglecting the ones of air conductivity. For formulas defined at given temperatures, a multiplicative factor k_i/k_i^{ref} is applied, where k_i is the ice thermal conductivity at the target temperature and k_i^{ref} is the ice conductivity value at the temperature at which the formula is valid (as used in, Gilbert et al., 2014; Zwinger et al., 2007). We found that this method works reasonably well, with only slightly higher deviations between estimations and computations at −60°C than at −3°C. Mean absolute errors and standard deviations from the Calonne formula are of 0.10 ± 0.12 $W{\cdot}m^{-1}{\cdot}K^{-1}$ at −60°C compared to 0.07 ± 0.07 $W{\cdot}m^{-1}{\cdot}K^{-1}$ at −3°C, for instance. Accounting for the temperature-dependency of ice conductivity seems thus overall

sufficient. This simplification could however not be evaluated at low densities, densities for which the contribution of the air conductivity might be more significant, given the relatively poor predictions of formulas in this density range. The SC model is the only formula that accounts for variations of the ice and air conductivities with temperature. It predicts that below 300 kg/m^3 the thermal conductivity no longer increases with decreasing temperature but decreases (switch from a predominant contribution of the ice conductivity to a predominant contribution of the air conductivity). This however does not fit our computations, for which this switch in the temperature effect is way less pronounced and occurs around 100 kg/m^3 (Figure 1b). To simply assess the contribution of air conductivity, we compared the SC estimates obtained with k_i and k_a at −3°C with the ones obtained with k_i at −3°C and k_a at −20°C and at −60°C. The latter options lead to thermal conductivity about 5% and 20% larger, respectively, within the density range 0–250 kg/m^3, differences that quickly vanish above. Accounting for the air contribution seems thus not primordial at first, except when focusing on light snow and when large temperature variations are considered.

3.5.3. Anisotropy

All the above formulas provide a single, isotropic value of thermal conductivity. This seems suitable for firn and porous ice but not for snow, for which thermal conductivity can be anisotropic and should then be described depending on orientations. Along this line, a density-based regression was suggested to access the vertical component of the thermal conductivity of depth hoar and faceted crystals specifically (Riche & Schneebeli, 2013). More convincingly, estimates of the vertical and horizontal thermal conductivity from density and structural anisotropy of the microstructure were presented by Löwe et al. (2013) and Calonne, Flin, et al. (2014). In particular, the SC model can be formulated for ellipsoidal inclusions, considering a transverse isotropic tensor of thermal conductivity, the degree of structural anisotropy being captured by the aspect ratio b/a of the ellipsoid (Giraud et al., 2007; Kushch & Sevostianov, 2014). This model was applied to snow during a temperature gradient metamorphism and reproduced reasonably well the evolution of the thermal conductivity in both vertical and horizontal directions and the development of anisotropy with time (Calonne et al., 2014). SC estimates of the vertical and horizontal components of thermal conductivity are written as follows:

$$k_{\mathrm{sc}_x} = k_{\mathrm{sc}_y} = k_{\mathrm{sc}_{xy}} = \frac{-(k_\mathrm{a}(\phi - Q) + k_\mathrm{i}((1-\phi) - Q)) - \sqrt{\triangle_{xy}}}{2(Q-1)} \tag{3}$$

$$k_{\mathrm{sc}_z} = \frac{-(k_\mathrm{a}(\phi - (1-2Q)) + k_\mathrm{i}((1-\phi) - (1-2Q))) - \sqrt{\triangle_z}}{2((1-2Q)-1)} \tag{4}$$

with

$$\triangle_{xy} = (k_\mathrm{a}(\phi - Q) + k_\mathrm{i}((1-\phi) - Q))^2 - 4(Q-1)Qk_\mathrm{i}k_\mathrm{a}$$

$$\triangle_z = (k_\mathrm{a}(\phi - (1-2Q)) + k_\mathrm{i}((1-\phi) - (1-2Q)))^2 - 4((1-2Q)-1)(1-2Q)k_\mathrm{i}k_\mathrm{a}$$

$$Q = \frac{1}{2(1-\gamma^2)}\left(1 - \frac{\gamma^2}{\sqrt{\gamma^2-1}}\tan^{-1}\left(\sqrt{\gamma^2-1}\right)\right) \quad \text{if } \gamma \geq 1$$

$$Q = \frac{1}{2(1-\gamma^2)}\left(1 - \frac{\gamma^2}{2\sqrt{1-\gamma^2}}\ln\left(\frac{1+\sqrt{1-\gamma^2}}{1-\sqrt{1-\gamma^2}}\right)\right) \quad \text{if } \gamma \leq 1$$

where γ is linked to the aspect ratio of the ellipsoid and the anisotropy ratio of k_{sc} by $\gamma = (a/b) \times \sqrt{k_{\mathrm{sc}_z}/k_{\mathrm{sc}_{xy}}}$. Here, we applied this SC model to our data, defining the aspect ratio based on the correlation lengths such as $b/a = \mathcal{A}_{l_\mathrm{c}}$. Overall, the estimated anisotropy ratios of thermal conductivity reproduce remarkably well the computed ones (Figure 2b).

3.6. A New Predictive Formulation

We aimed here at providing a single formulation to allow for robust estimates of thermal conductivity over the complete density range 0–917 kg/m^3 and for any temperature conditions, so it could be used for snow, firn, and porous ice in alpine or polar conditions. To do so, we combined the firn linear regression equation (1), which describes the density-conductivity relationship $k^{\mathrm{ref}}_{\mathrm{firn}}(\rho)$ in firn at −3°C, and the quadratic regression of Calonne et al. (2011), which describes the density-conductivity relationship $k^{\mathrm{ref}}_{\mathrm{snow}}(\rho)$ in snow at −3°C. The contribution of these two regressions are determined by a weight factor θ that depends on the

current density with respect to a transition density value. The temperature effect is taken into account by multiplicative factors that reflect the variations of air and ice conductivity with temperature compared with their values at −3°C. The new formulation reads

$$k_{\text{snow-firn}}(\rho, T) = (1-\theta)\frac{k_i(T)k_a(T)}{k_i^{\text{ref}}k_a^{\text{ref}}}k_{\text{snow}}^{\text{ref}}(\rho) + \theta\frac{k_i(T)}{k_i^{\text{ref}}}k_{\text{firn}}^{\text{ref}}(\rho) \quad (5)$$

with

$$\theta = 1/\left(1+\exp(-2a(\rho-\rho_{\text{transition}}))\right)$$
$$k_{\text{firn}}^{\text{ref}}(\rho) = 2.107 + 0.003618(\rho-\rho_i)$$
$$k_{\text{snow}}^{\text{ref}}(\rho) = k_{\text{cal.}} = 0.024\text{–}1.23\times10^{-4}\rho + 2.5\times10^{-6}\rho^2$$

where $k_i(T)$ and $k_a(T)$ are the ice and air conductivity at the temperature T, $k_i^{\text{ref}} = 2.107\ \text{W·m}^{-1}\text{·K}^{-1}$ and $k_a^{\text{ref}} = 0.024\ \text{W·m}^{-1}\text{·K}^{-1}$ are the ice and air conductivities at the reference temperature T_{ref} of −3°C, respectively, $a = 0.02\ \text{m}^3/\text{kg}$, and $\rho_{\text{transition}} = 450\ \text{kg/m}^3$ (value providing the best match with our computations) corresponds to the density value at which the major contribution switches between $k_{\text{snow}}^{\text{ref}}$ and $k_{\text{firn}}^{\text{ref}}$.

Estimates from equation (5) are shown in Figures 1–3. Additional description of the errors can be found in the supporting information (Figure S1 and Table S2). Estimates follow closely the computed values, performing better than any of the parameterizations or model presented earlier. The mean absolute error and standard deviation are very low, $0.02 \pm 0.02\ \text{W·m}^{-1}\text{·K}^{-1}$ at −3°C and of $0.02 \pm 0.03\ \text{W·m}^{-1}\text{·K}^{-1}$ at −60°C. Performances are consistent throughout the density range, with errors that do not exceed $0.05\ \text{W·m}^{-1}\text{·K}^{-1}$ at −3°C and $0.12\ \text{W·m}^{-1}\text{·K}^{-1}$ at −60°C, and relative errors less than ±25%. One exception concerns density below 150 kg/m^3 where relative errors are up to −40%, as already pointed out for the Calonne formula. One advantage of this new formulation is that the Calonne formula implemented to describe the thermal conductivity of snow with density can be easily replaced by a future, more suitable formulation.

4. Conclusions

The tensor of effective thermal conductivity at −3, −20, and −60°C, obtained by 3-D images-based computations, is presented for 27 firn and porous ice samples from cold sites in Antarctica and for 37 seasonal snow samples. The evolution of the thermal conductivity over a wide range of density from fresh snow to bubbly ice is then revealed. Averaged values range from 0.06 to $2.00\ \text{W·m}^{-1}\text{·K}^{-1}$ for densities from 102 to 888 kg/m^3.

We reported that (1) the thermal conductivity of firn and porous ice can be very well estimated based on a linear relationship with density ($R^2 = 0.99$, standard deviation = $10^{-5}\ \text{W·m}^{-1}\text{·K}^{-1}$), contrasting with the quadratic and more scattered correlation reported for snow, (2) no or very little anisotropy was observed for firn and porous ice, indicating that a single, orientationally averaged conductivity value is sufficient to describe heat fluxes in any direction, again in contrast with snow for which modeling of the vertical and horizontal component of the thermal conductivity can be necessary, and (3) temperature greatly influences thermal conductivity of firn and porous ice, the influence above 600 kg/m^3 being already about the one observed in pure ice, for example, an increase of about 35% is reported from −3 to −60°C in this density range. Accounting for the variations of ice conductivity with temperature seems overall sufficient, except for light snow subjected to large temperature fluctuations for which the contribution of air conductivity variations should also be considered.

Comparing our results to predictive formulas of thermal conductivity used in heat transfer modeling of alpine and polar glaciers, none of the formulas allowed for robust estimations throughout the density range. In particular, snow-designed parameterizations provide underestimated values, up to −30%, when applied to firn and porous ice. The analytical SC model provides overall fair estimates and, most remarkably, allows capturing the anisotropy of thermal conductivity. We present a new density- and temperature-based formula to accurately estimate isotropic thermal conductivity of snow, firn, and porous ice in alpine or polar conditions. Further studies should be undertaken to confront our findings to different polar and alpine environments than the Antarctic cold accumulation zone condition investigated here. Our research offers new opportunities to improve heat transfer modeling in glaciers and ice sheets.

Acknowledgments
The data presented in this paper are available online (https://doi.pangaea.de/10.1594/PANGAEA.906906). We greatly thank Sergey Marchenko for kindly providing his data set of thermal conductivity obtained at Lomonosovfonna, Svalbard. The 3SR lab is part of the Labex Tec 21 (Investissements d'Avenir, Grant Agreement ANR-11-LABX-0030). CNRM/CEN and IGE are part of Labex OSUG@2020 (Investissements d'Avenir, Grant ANR-10-LABX-0056). Authors acknowledge the Labex CEMAM (Center of Excellence of Multifunctional Architectured Materials, "Investments for the Future" Program, Grant ANR-10-LABX-44-01) for its contribution for the funding of the X-ray tomography equipment. This work has been also supported by a grant from Labex OSUG@2020 (Investissements d'Avenir—ANR-10-LABX-0056). We also thank the ID19 beamline of the ESRF for the acquisition of several tomographic images used in this study. We greatly thank Adrien Gilbert and an anonymous reviewer for their comments, which improved the manuscript quality.

References

Arthern, R. J., & Wingham, D. J. (1998). The natural fluctuations of firn densification and their effect on the geodetic determination of ice sheet mass balance. *Climatic Change*, *40*(3-4), 605–624.

Auriault, J.-L., Boutin, C., & Geindreau, C. (2009). *Homogenization of coupled phenomena in heterogenous media*. London: Wiley-ISTE.

Barnola, J.-M., Pimienta, P., Raynaud, D., & Korotkevich, Y. S. (1991). CO_2-climate relationship as deduced from the Vostok ice core: A re-examination based on new measurements and on a re-evaluation of the air dating. *Tellus B*, *43*(2), 83–90.

Brucker, L., Picard, G., Arnaud, L., Barnola, J.-M., Schneebeli, M., Brunjail, H., et al. (2011). Modeling time series of microwave brightness temperature at Dome C, Antarctica, using vertically resolved snow temperature and microstructure measurements. *Journal of Glaciology*, *57*(201), 171–182.

Bruggeman, V. D. (1935). Berechnung verschiedener physikalischer Konstanten von heterogenen Substanzen. I. Dielektrizitätskonstanten und Leitfähigkeiten der Mischkörper aus isotropen Substanzen. *Annalen der physik*, *416*(7), 636–664.

Burr, A., Ballot, C., Lhuissier, P., Martinerie, P., Martin, C. L., & Philip, A. (2018). Pore morphology of polar firn around closure revealed by X-ray tomography. *The Cryosphere*, *12*(7), 2481–2500.

Burr, A., Lhuissier, P., Martin, C. L., & Philip, A. (2019). In situ X-ray tomography densification of firn: The role of mechanics and diffusion processes. *Acta Materialia*, *167*, 210–220.

Calonne, N., Flin, F., Geindreau, C., Lesaffre, B., & Rolland du Roscoat, S. (2014). Study of a temperature gradient metamorphism of snow from 3-D images: Time evolution of microstructures, physical properties and their associated anisotropy. *The Cryosphere*, *8*(6), 2255–2274.

Calonne, N., Flin, F., Morin, S., Lesaffre, B., du Roscoat, S. R., & Geindreau, C. (2011). Numerical and experimental investigations of the effective thermal conductivity of snow. *Geophysical Research Letters*, *38*, L23501. https://doi.org/10.1029/2011GL049234

Calonne, N., Geindreau, C., & Flin, F. (2014). Macroscopic modeling for heat and water vapor transfer in dry snow by homogenization. *The Journal of Physical Chemistry B*, *118*(47), 13393–403.

Coléou, C., & Barnola, J.-M. (2001). 3-D snow and ice images by X-ray microtomography. *ESRF Newsletter*, *35*, 24–26.

Coléou, C., Lesaffre, B., Brzoska, J.-B., Ludwig, W., & Boller, E. (2001). Three-dimensional snow images by X-ray microtomography. *Annals of Glaciology*, *32*, 75–81.

Cummings, E., Johnson, J., & Brinkerhoff, D. (2013). Development of a finite element firn densification model for converting volume changes to mass changes. arXiv e-print. Retrieved from https://arXiv.org/abs/1308.6616

Dahl-Jensen, D., Mosegaard, K., Gundestrup, N., Clow, G. D., Johnsen, S. J., Hansen, A. W., & Balling, N. (1998). Past temperatures directly from the Greenland ice sheet. *Science*, *282*, 268–271.

Fierz, C., Armstrong, R. L., Durand, Y., Etchevers, P., Greene, E., McClung, D. M., et al. (2009). The international classification for seasonal snow on the ground. *IHP-VII Technical Documents in Hydrology N°83*. Paris: IACS Contribution N°1, UNESCO-IHP.

Flin, F., Brzoska, J. B., Lesaffre, B., Coleou, C., & Pieritz, R. A. (2004). Three-dimensional geometric measurements of snow microstructural evolution under isothermal conditions. *Annals of glaciology*, *38*, 39–44.

Flin, F., Lesaffre, B., Dufour, A., Gillibert, L., Hasan, A., Rolland du Roscoat, S., et al. (2011). On the computations of specific surface area and specific grain contact area from snow 3-D images. In Furukawa, Y. (Ed.), *Proceedings of the 12th International Conference on the Physics and Chemistry of Ice held (PCI 2010)* (pp. 321–328). Sapporo, JP: Hokkaido University Press.

Fukusako, S. (1990). Thermophysical properties of ice, snow, and sea ice. *International Journal of Thermophysics*, *11*(2), 353–372.

Funk, M., Echelmeyer, K., & Iken, A. (1994). Mechanisms of fast flow in Jakobshavns isbræ, west Greenland: Part II. Modeling of englacial temperatures. *Journal of Glaciology*, *40*(136), 569–585.

Gautier, E., Savarino, J., Erbland, J., Lanciki, A., & Possenti, P. (2016). Variability of sulfate signal in ice core records based on five replicate cores. *Climate of the Past*, *12*(1), 103–113.

Giese, A. L., & Hawley, R. L. (2015). Reconstructing thermal properties of firn at Summit, Greenland, from a temperature profile time series. *Journal of Glaciology*, *61*(227), 503–510.

Gilbert, A., Flowers, G. E., Miller, G. H., Rabus, B. T., Van Wychen, W., Gardner, A. S., & Copland, L. (2016). Sensitivity of Barnes ice cap, Baffin Island, Canada, to climate state and internal dynamics. *Journal of Geophysical Research: Earth Surface*, *121*, 1516–1539. https://doi.org/10.1002/2016JF003839

Gilbert, A., Gagliardini, O., Vincent, C., & Wagnon, P. (2014). A 3-D thermal regime model suitable for cold accumulation zones of polythermal mountain glaciers. *Journal of Geophysical Research: Earth Surface*, *119*, 1876–1893. https://doi.org/10.1002/2014JF003199

Gilbert, A., Leinss, S., Kargel, J., Kääb, A., Gascoin, S., Leonard, G., et al. (2018). Mechanisms leading to the 2016 giant twin glacier collapses, Aru Range, Tibet. *Cryosphere*, *12*(9), 2883–2900.

Gilbert, A., & Vincent, C. (2013). Atmospheric temperature changes over the 20th century at very high elevations in the European Alps from englacial temperatures. *Geophysical Research Letters*, *40*, 2102–2108. https://doi.org/10.1002/grl.50401

Gilbert, A., Vincent, C., Gagliardini, O., Krug, J., & Berthier, E. (2015). Assessment of thermal change in cold avalanching glaciers in relation to climate warming. *Geophysical Research Letters*, *42*, 6382–6390. https://doi.org/10.1002/2015GL064838

Gilbert, A., Wagnon, P., Vincent, C., Ginot, P., & Funk, M. (2010). Atmospheric warming at a high-elevation tropical site revealed by englacial temperatures at Illimani, Bolivia (6340 m above sea level, 16°S, 67°W). *Journal of Geophysical Research*, *115*, D10109. https://doi.org/10.1029/2009JD012961

Giraud, A., Gruescu, C., Do, D. P., Homand, F., & Kondo, D. (2007). Effective thermal conductivity of transversely isotropic media with arbitrary oriented ellipsoidal inhomogeneities. *International Journal of Solids and Structures*, *44*(9), 2627–2647.

Goujon, C., Barnola, J.-M., & Ritz, C. (2003). Modeling the densification of polar firn including heat diffusion: Application to close-off characteristics and gas isotopic fractionation for Antarctica and Greenland sites. *Journal of Geophysical Research*, *108*(D24), 4792. https://doi.org/10.1029/2002JD003319

Hill, R. (1965). A self-consistent mechanics of composite materials. *Journal of the Mechanics and Physics of Solids*, *13*(4), 213–222.

Hills, B. H., Harper, J. T., Meierbachtol, T. W., Johnson, J. V., Humphrey, N. F., & Wright, P. J. (2018). Processes influencing heat transfer in the near-surface ice of Greenland's ablation zone. *The Cryosphere*, *12*(10), 3215–3227.

Humphrey, N. F., Harper, J. T., & Pfeffer, W. T. (2012). Thermal tracking of meltwater retention in Greenland's accumulation area. *Journal of Geophysical Research*, *117*, F01010. https://doi.org/10.1029/2011JF002083

Kaempfer, T. U., Schneebeli, M., & Sokratov, S. A. (2005). A microstructural approach to model heat transfer in snow. *Geophysical Research Letters*, *32*, L21503. https://doi.org/10.1029/2005GL023873

Kanit, T., N'Guyen, F., Forest, S., Jeulin, D., Reed, M., & Singleton, S. (2006). Apparent and effective physical properties of heterogeneous materials: Representativity of samples of two materials from food industry. *Computer Methods in Applied Mechanics and Engineering*, *195*(33-36), 3960–3982.

Kushch, V. I., & Sevostianov, I. (2014). Dipole moments, property contribution tensors and effective conductivity of anisotropic particulate composites. *International Journal of Engineering Science*, *74*, 15–34.
Lüthi, M. P., & Funk, M. (2001). Modelling heat flow in a cold, high-altitude glacier: Interpretation of measurements from Colle Gnifetti, Swiss Alps. *Journal of Glaciology*, *47*(157), 314–324.
Larour, E., Seroussi, H., Morlighem, M., & Rignot, E. (2012). Continental scale, high order, high spatial resolution, ice sheet modeling using the ice sheet system model (ISSM). *Journal of Geophysical Research*, *117*, F01022. https://doi.org/10.1029/2011JF002140
Lomonaco, R., Albert, M., & Baker, I. (2011). Microstructural evolution of fine-grained layers through the firn column at Summit, Greenland. *Journal of Glaciology*, *57*(204), 755–762.
Löwe, H., Riche, F., & Schneebeli, M. (2013). A general treatment of snow microstructure exemplified by an improved relation for thermal conductivity. *The Cryosphere*, *7*(5), 1473–1480.
Marchenko, S., Cheng, G., Lötstedt, P., Pohjola, V., Pettersson, R., van Pelt, W., & Reijmer, C. (2019). Thermal conductivity of firn at Lomonosovfonna, Svalbard, derived from subsurface temperature measurements. *The Cryosphere*, *13*(7), 1843–1859.
Mellor, Malcolm (1977). Engineering properties of snow. *Journal of Glaciology*, *19*(81), 15–66.
Morin, S., Domine, F., Dufour, A., Lejeune, Y., Lesaffre, B., Willemet, J.-M., et al. (2013). Measurements and modeling of the vertical profile of specific surface area of an alpine snowpack. *Advances in Water Resources*, *55*, 111–120.
Morin, S., Erbland, J., Savarino, J., Domine, F., Bock, J., Friess, U., et al. (2012). An isotopic view on the connection between photolytic emissions of NO_x from the Arctic snowpack and its oxidation by reactive halogens. *Journal of Geophysical Research*, *117*, D00R08. https://doi.org/10.1029/2011JD016618
Paterson, W. S. B. (1994). *The physics of glaciers*. Oxford: Butterworth-Heinemann.
Reijmer, C. H., & Hock, R. (2008). Internal accumulation on Storglaciären, Sweden, in a multi-layer snow model coupled to a distributed energy-and mass-balance model. *Journal of Glaciology*, *54*(184), 61–72.
Riche, F., & Schneebeli, M. (2013). Thermal conductivity of snow measured by three independent methods and anisotropy considerations. *The Cryosphere*, *7*(1), 217–227.
Salamatin, A. N., Lipenkov, V. Y., Barkov, N. I., Jouzel, J., Petit, J. R., & Raynaud, D. (1998). Ice core age dating and paleothermometer calibration based on isotope and temperature profiles from deep boreholes at Vostok station (East Antarctica). *Journal of Geophysical Research*, *103*(D8), 8963–8977.
Satyawali, P. K., & Singh, A. K. (2008). Dependence of thermal conductivity of snow on microstructure. *Journal of Earth System Sciences*, *117*(4), 465–475.
Schneebeli, M., & Sokratov, S. A. (2004). Tomography of temperature gradient metamorphism of snow and associated changes in heat conductivity. *Hydrological Processes*, *18*(18), 3655–3665.
Schwander, J., Sowers, T., Barnola, J.-M., Blunier, T., Fuchs, A., & Malaizé, B. (1997). Age scale of the air in the summit ice: Implication for glacial-interglacial temperature change. *Journal of Geophysical Research*, *102*(D16), 19,483–19,493.
Schwerdtfeger, P. (1963). Theoretical derivation of the thermal conductivity and diffusivity of snow. *International Association of Hydrological Sciences Publication*, *61*, 75–81.
Seddik, H., Greve, R., Zwinger, T., Gillet-Chaulet, F., & Gagliardini, O. (2012). Simulations of the Greenland ice sheet 100 years into the future with the full Stokes model Elmer/Ice. *Journal of Glaciology*, *58*(209), 427–440.
Sturm, M., Holmgren, J., König, M., & Morris, K. (1997). The thermal conductivity of seasonal snow. *Journal of Glaciology*, *43*(143), 26–41.
Thoemen, H., Walther, T., & Wiegmann, A. (2008). 3D simulation of macroscopic heat and mass transfer properties from the microstructure of wood fibre networks. *Composites Science and Technology*, *68*(3–4), 608–616.
Torquato, S. (2002). *Random heterogeneous materials: Microstructure and macroscopic properties*. New York: Springer-Verlag.
Van Dusen, M. S., & Washburn, E. W. (1929). Thermal conductivity of non-metallic solids, *International critical tables of numerical data, physics, chemistry and technology* (Vol. 5, pp. 216–217). New York: McGraw-Hill.
Van Ommen, T. D., Morgan, V. I., Jacka, T. H., Woon, S., & Elcheikh, A. (1999). Near-surface temperatures in the Dome Summit South (Law Dome, East Antarctica) borehole. *Annals of Glaciology*, *29*, 141–144.
Yen, Y.-C. (1981). Review of the thermal properties of snow, ice and sea ice (Tech. Rep. No. 81-10). Hanover, NH: Cold Regions Research and Engineering Laboratory.
Zwinger, T., Greve, R., Gagliardini, O., Shiraiwa, T., & Lyly, M. (2007). A full Stokes-flow thermo-mechanical model for firn and ice applied to the Gorshkov crater glacier, Kamchatka. *Annals of Glaciology*, *45*, 29–37.